Applied Surface Science 521 (2020) 146360

Contents lists available at ScienceDirect

Applied Surface Science

journal homepage: www.elsevier.com/locate/apsusc

Effect of cobalt-based coating microstructure on the thermal fatigue performance of AISI H13 hot work die steel

Xudong Yang[a], Chuanwei Li[a,b,*], Ziyang Zhang[a], Xinyu Zhang[a], Jianfeng Gu[c,d,*]

[a] Institute of Materials Modification and Modeling, School of Materials Science and Engineering, Shanghai Jiao Tong University, Shanghai 200240, China
[b] Shanghai Key Laboratory of Materials Laser Processing and Modification, Shanghai Jiao Tong University, Shanghai 200240, China
[c] Collaborative Innovation Center for Advanced Ship and Deep Sea Exploration, Shanghai Jiao Tong University, Shanghai 200240, China
[d] Materials Genome Initiative Center, Shanghai Jiao Tong University, Shanghai 200240, China

ARTICLE INFO

Keywords:
Co-based coating
Direct laser deposition (DLD)
Thermal-fatigue (TF) life
γ/ε transformation
Stacking fault (SF) energies

ABSTRACT

The Co-based coating by laser deposition could improve the thermal-fatigue (TF) resistance of hot working dies but the effect of technology on properties remained to be studied further. This work investigated the influence of the microstructure and γ/ε transformation on the TF life of the Co-based coating of the AISI H13 hot work die steel. Direct laser deposition (DLD) layers were prepared on the steel surface using modified Co-based alloys, which increased the contents of Cr, W, and Ni. The single and duplex layers were made under precise conditions, and the difference in the TF test life was significant. Meanwhile, the hardness of the duplex layer coating was much higher than that of the single one in the TF process consistently. Various detection methods were adopted to characterize the Co-based coating structures and crack propagation during the TF test. The microstructure of the two deposition coatings uniformly included the γ-Co phase and $M_{23}C_6$ crystalline phase. Moreover, after the TF experiment, the γ/ε transformation only occurred in the single layer as observed by transmission electron microscopy and electron backscattered diffraction. This indicated that the dilution of the base metal element distribution played a key role in reducing the stability of the γ-Co phase, which resulted in relatively low stacking fault (SF) energies, micro-hardness, a high fraction of the precipitate, and an early crack generation of the coating. This research was beneficial for understanding the microstructure, grain growth, γ/ε transformation, and crack propagation behavior in the DLD layers and TF test.

1. Introduction

The aluminum die-casting mold has gained increasing importance for automotive applications due to its high quality, efficiency, and low cost [1]. The surface of the hot-work die-steel suffers from the pressurized thermal impact on molten aluminum (about 600 °C) and the cold impact of water [2]. Under exposure to harsh environments, the die is repeatedly subjected to cyclic strain or stress caused by thermal loadings, which is responsible for the significant damage. Traditional steel such as AISI H13 loses efficacy quite early in their lifetime due to thermal fatigue (TF), corrosion, and abrasion [3]. Many studies have been conducted to improve the resistance of the base metal, including nitriding [2], laser quenching [4], laser remelting [5], laser deposition [6], and surface alloying [1] All these methods indicate that a certain degree of increase in the hardness and oxidation resistance results in enhanced resistance to TF, although the mechanisms are different [1–6].

As one of the additive manufacturing technologies, direct laser deposition (DLD) is used for the rapid prototyping or production of 3D objects, which were controlled by computer-aided manufacturing (CAM)[7]. DLD is a surface modification technique that makes use of laser energy to rapidly melt and solidify die materials to obtain a design-structure with excellent properties [8,9]. Compared with traditional nitriding, surface alloy, and heat treatment techniques, DLD is more efficient and manageable as it offers the capability to control the surface morphology, roughness, and mechanical performance by parameter modification [10]. Thus, a variety of superiorities owing to the adjustment could be gained, such as the metallurgical bonding between the cladding and substrate, dilution rate, dense microstructure, temperature gradient, non-equilibrium phases, and supersaturated solid solutions [11].

Co-based coating, as a hard-facing alloy, is extensively used in hot-work die materials owing to its excellent resistance to corrosion, abrasion, and excellent hardness in both room and elevated

* Corresponding authors at: School of Materials Science and Engineering, Shanghai Jiao Tong University, Shanghai 200240, China.
E-mail addresses: li-chuanwei@sjtu.edu.cn (C. Li), gujf@sjtu.edu.cn (J. Gu).

https://doi.org/10.1016/j.apsusc.2020.146360
Received 21 October 2019; Received in revised form 7 April 2020; Accepted 16 April 2020
Available online 25 April 2020
0169-4332/

temperatures [12]. During the cooling process, the phase transformation from the face-centered cubic (fcc) (γ-Co) phase to the hexagonal close-packed (hcp) (ε-Co) phase has been investigated and it could be regarded as the strain-induced martensitic transformations (SIMTs) of the γ-Co phase owing to the low stacking fault (SF) energies [12–14]. The high cooling velocity and fcc stabilization elements make it possible to maintain a complete γ-Co phase at room temperature without any ε phase. Lee et al. [13] annealed the Co-Cr-Mo-N alloy at 1473 K for 1 h and cooled it to room temperature in a furnace. The uniaxial tensile tests showed that the grain boundaries and phase boundaries acted as nucleation sites for the SIMTs and for the crack initiation.

As one of the main causes of failure of the hot-work die-mold, TF is always induced by a rapid change in temperature during pressure casting operations [15]. L. Emanuelli et al. [16] reported that a decrease in the Co-based binder content increases the TF crack propagation for the WC-Co alloy coating. The behaviors of Co-29Cr-6Mo during the strain-controlled iso-thermal fatigue test were also reported [17]. The results indicated that the cracks nucleated along the planar slip on the surface at a low temperature; however, the high oxidation aggravated the TF damage at 700 °C, and the cracks extended to a mixed form of intergranular and transgranular fracture. According to the research from Y. Wu et al. [18], cracks mainly occur in net-like eutectic structures and γ/ε interfaces for the TF experiment of Stellite 6 (Co-Cr alloy) coating. Some reports concentrated on the development of cracks, and it was revealed that O atoms diffuse into the substrate through the early micro-cracks and assume a V shape along with the rough reduction [19–21].

This study aims to enhance the TF resistance by fabricating single and duplex Co-based deposition layers on the H13 hot-work die steel through DLD. Many studies have revealed that the cracks appear at the grain boundaries and γ/ε interfaces, although few studies have demonstrated how to modify the microstructure or chemical component to improve the TF lifetime. The objective of this article is to better understand the trend to prolong the TF life through the composition design of Co-based metal powder and by modulating the DLD parameter. Various investigations have focused on the crystal structure and crack performance. Meanwhile, the mechanism of the crack propagation is also described based on the experiments.

2. Material and methods

2.1. Materials and DLD process

A 15-mm-thick AISI H13 steel was used as the substrate, and the chemical composition was listed in Table 1. The H13 plate was ground and cleaned with acetone and alcohol prior to the experiment. The deposition materials were designed based on the characteristics of the adding-elements, Ni could increase SF energies obviously and W, Ru could decrease the SF energies [22]. As shown in Fig. 1(a), spherical gas-atomized Co-based powders had diameters between 50 and 100 μm and the content is listed in Table 2. DLD was performed using an ytterbium fiber laser (YLS-2000, IPG, America) with a wavelength of 1070 nm, laser focus size of 0.8 mm. The coating was fabricated by the melting and solidification of the powder, which was exported through a coaxial nozzle with argon shielding gas protection at 12 L/min, as illustrated in Fig. 1(b). As shown in Fig. 1(c), the scanning strategy was snake-shaped and the parameters for the DLD single layer include the following: laser power (P) = 800 W, scanning velocity (v) = 6 mm/s, and defocusing (d) = 5 mm. The first-layer deposition parameters were the same as the single layer, and the second layer was fabricated by decreasing the scanning speed to 4 mm/s while the other factors remain the same.

Table 1
Chemical compositions of H13 steel (wt. %).

Element	C	Cr	Mo	Si	V	Mn	P	S	Fe
Chemical composition	0.37	5.13	1.23	0.95	0.83	0.36	0.009	0.001	Bal.

2.2. Thermal fatigue test and micro-hardness

The TF test was carried out using a home-made device, and the sketch is revealed in Fig. 2(a) and (b). The sample was machined in a particular shape of the geometry shown in Fig. 2(c). In addition, the two sample-types were machined in the same deposition thickness of about 500 μm for subtracting the impacts on the thickness on the properties, such as wetting-spreading [23] and wear behavior [24]. During the TF experiment, which was similar to the industrial production, with external induction, the surface of the specimen was heated to 600 °C (± 3 °C) in < 5.5 s and cooled to room temperature with jetted water in 10 s. The DLD layer was also ground and polished to reduce the influence of roughness and pollution prior to the TF treatment. The laser deposition surface shifted toward the water direction and maintained the same location for different samples. The variation in the micro-hardness of the two types of DLD layers and the TF test samples were measured using the HM T4 XYprog Vickers micro-hardness tester (Helmut Fischer GmbH) with a load of 0.3 kg and a holding time of 5 s.

2.3. Characterization

For the purpose of microstructure observation including the TF crack initiation and propagation, all the specimens were processed into blocks with dimension of 20 mm × 6 mm × 5 mm by wire cut electrical discharge machining. Then the samples were ground and polished by standard metallographic techniques with a polishing machine (Automet 300, Buehler, America) and etched by aqua regia (vol. 25% HNO_3 and vol. 75% HCL). An optical microscope (OM, Axio Observer.A1m, Zeiss, Germany) and a scanning electron microscope (LYRA3 GMU, TESCAN, Czech Republic) equipped with an energy dispersive spectroscope (EDS, Aztec X-Max80, Oxford, the United Kingdom) and an electron backscatter diffraction (EBSD, HKL NordlysMax3, Oxford, the United Kingdom) instrument were used to characterize the microstructure of the composite. The step size was 0.15 μm and the voltage was 20 kV. The X-ray diffraction patterns (XRD, Ultima IV, Rigaku, Japan) were recorded using Cu Kα radiation with a wavelength of λ_{Cu} = 1.5406 Å. Furthermore, a 2θ angular range varying from 10° to 90° was determined to confirm the phase and the scanning velocity was 5°/min. Transmission electron microscopy (TEM, JEM2100F, JEOL, Japan) was used to investigate the microstructures on an enhanced subtle level, and the specimens were prepared by a focused ion beam (FIB, LYRA3 GMU, TESCAN, Czech Republic).

3. Results

3.1. Microstructures and phase constituents

Fig. 3(a) shows the cross-section of the DLD double layer along the laser scanning direction. The deposition consisted of columnar, cellular, and dendritic regions from the substrate to the surface, which were similar to those of the single layer in Fig. 3(e)[25]. The columnar grains were perpendicular to the substrate due to the rapid heat dissipation, and the microstructure transformed into those of the cellular and dendritic grains with the reduction of the temperature gradient (Fig. 3(b), (c), (f), (g), and (h))[26]. The noticeable boundary of the two layers was labeled with a white line in Fig. 3(d). The latter deposition was required to ensure that parts of the prior layer melted except for the columnar area, and this could reduce the stress concentration on the junction according to previous researches [27–29]. At relatively high magnifications (Fig. 4(a) and (b)), it is evident that the microstructures exhibit two phases: grey matrix and white net-like precipitates, which

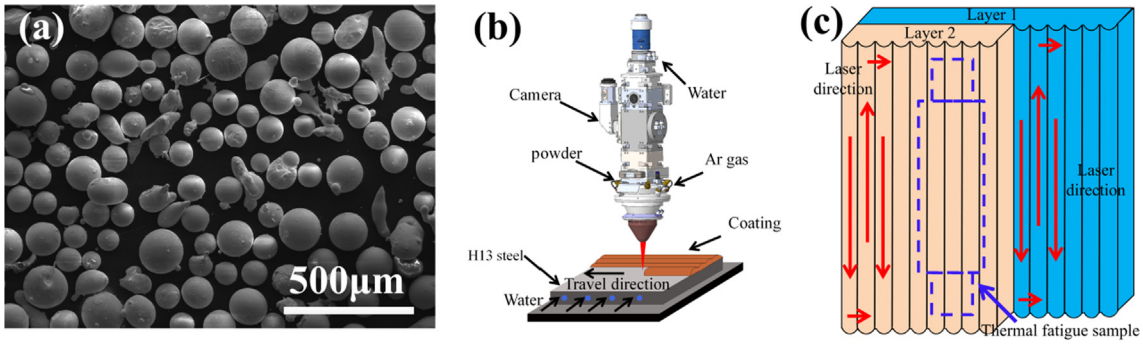

Fig. 1. (a) The morphology of the Co-based powder; (b) schematic diagram of the DLD process; (c) depositing direction of two layers coatings.

Table 2
Chemical compositions of Co-based powder (wt. %).

Element	Cr	Ni	W	C	Si	Fe	Co
Chemical composition	25.7	22.8	12.5	0.7	1.2	1.2	Bal.

were distributed among the grain boundaries. The percentage of white phase was identified by different colors through Photoshop software. The white phase was 10% of the total region in the double layer and 16% in the single one.

The results of the EDS analysis for the TF samples surfaces are shown in Fig. 4(c)–(f) and the detail compositions are listed in Table 3. Identically, the two deposition layers contained a Co matrix (points B and D) and carbides (points A and C), which had a higher percentage of W and Cr compared to the base metal. Notably, Fe was relatively high in the single layer, whether in the matrix or precipitate phase. This indicated that the contents of the H13 base metal diffused into the cladding, and the case was particularly distinct from the single layer. Moreover, Fe influenced the stability reduction of the matrix [30]. Eventually, Fig. 5(a)–(f) include the SEM images and element distributions of the double layer. The white line separated the two layers, and it is noticeable that the second cladding could impede the blending of steel. According to Fig. 5(g)–(l), single cladding suffered the elements diffusion from substrate.

According to the elemental distribution maps, the dividing line of the different layers could be labeled in the duplex cladding (Fig. 6(a)–(c)). The inverse pole figure (IPF) and local misorientation (LMO) maps show that the perfect bonding between the two layers and the residual stress were concentrated on the grain boundaries instead of the two claddings. Moreover, due to the poor quality of the Kikuchi diffraction pattern, the dark area revealed the internal boundaries or precipitates, which were visible around the matrix [31]. The phase maps (Fig. 6(b)) display that the coating was composed of the γ-Co matrix and precipitate phases, which could be confirmed further. The LMO maps represent the misorientation angle between all contiguous sites in or at the grain boundaries, and it indicates the residual plastic strain on the substrate [32]. From Fig. 6(c), the results confirmed that the strain in the boundary was higher than that in the grain interior and a tiny deformation or slip occurred in the interface of the precipitate/matrix, which caused a crack to occur [33].

For the single layer, the growth of the juncture in the grain obeyed the orientation of the previous cladding (Fig. 6(d)) and only the γ-Co matrix can be found to be similar to that of the double layer (Fig. 6(e)). Furthermore, the residual plastic strain was also concentrated on the grain boundaries unevenly due to the existence of precipitates in the boundaries (Fig. 6(f)).

A representative TEM analysis of the double cladding is illustrated in Fig. 7(a)–(c). The bright-field TEM images and selected area electron diffraction (SEAD) patterns showed that the matrix in the deposition

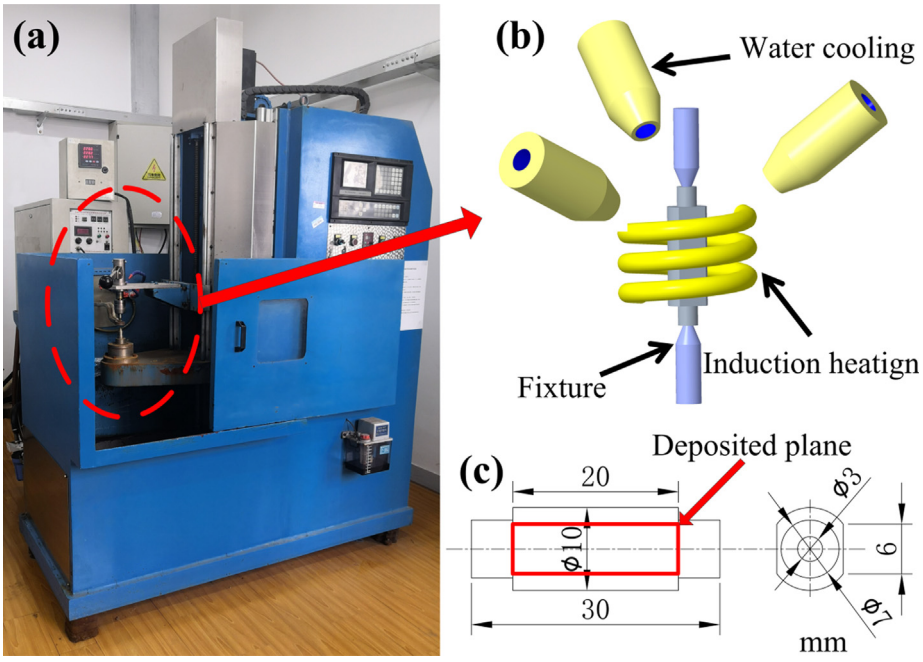

Fig. 2. (a) and (b) TF tester illustration. (c) Geometry of the TF specimen.

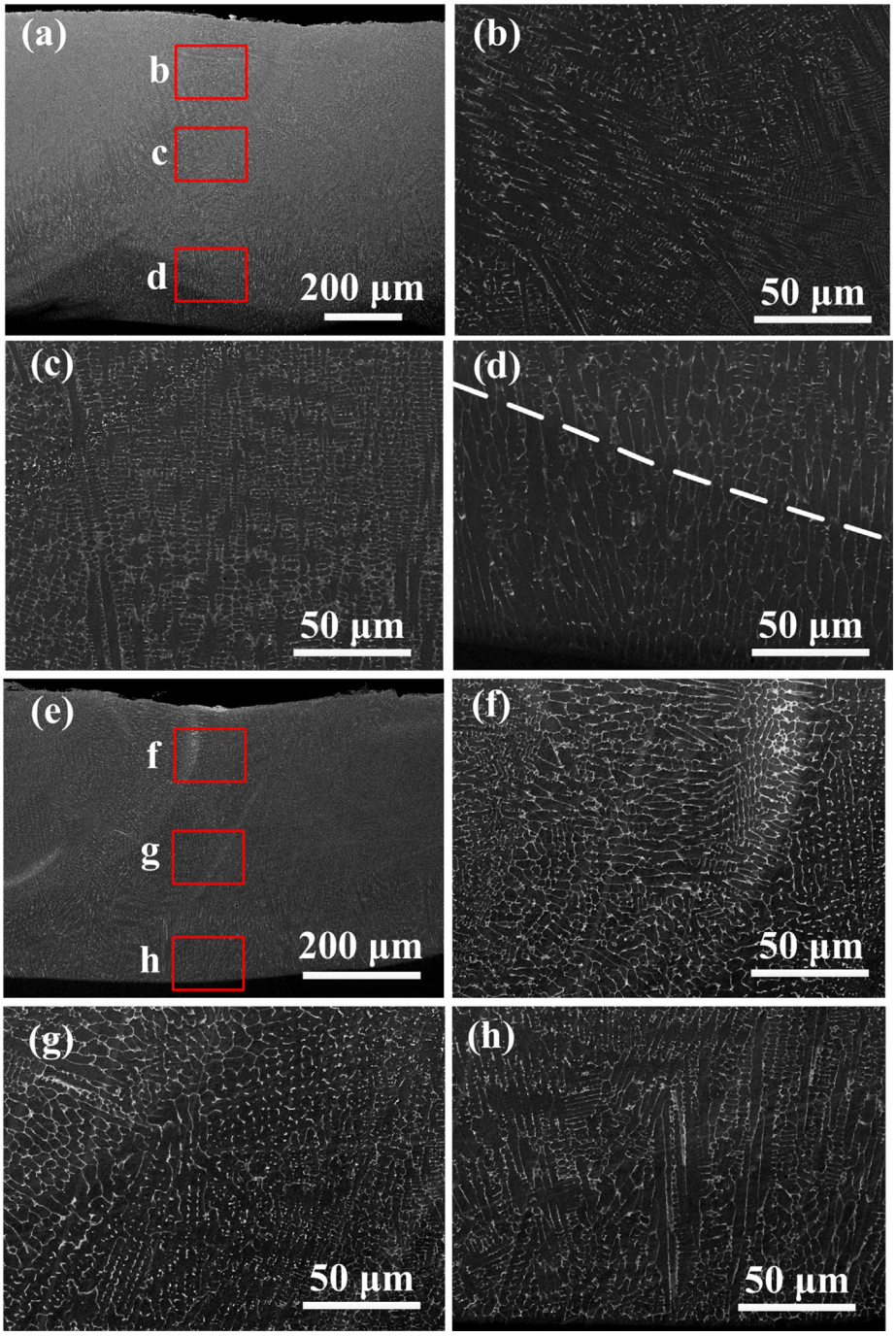

Fig. 3. SEM images showing the deposition microstructure of the cross-section, cellular, dendritic, and columnar grains. (a–d) for the double layer and (e–h) for the single layer.

layer was a typical γ-Co and the precipitate along the boundary was $M_{23}C_6$, whose zone axes were [0 0 1] and [0$\bar{1}$1]. The EDS spectra in Fig. 7(g)–(l) illustrate that the matrix contained Co, Ni, and Fe mainly, and the W and Cr distributed in the precipitation aggravated the carbide formation. The phenomenon indicated that the aggregation of the carbide forming elements resulted from the solid solubility limitation of supersaturated solid solution and the low formation energy at the γ-Co interface, which is in accord with previous research [18]. The $M_{23}C_6$ precipitate separated the Co matrix, which led to the instability of the intergranular fracture of the cladding [34]. This factor helped to understand the TF mechanism. The same analysis was applied to the single layer, and the compositions contained γ-Co and $M_{23}C_6$ phases, as shown in Fig. 7(d)–(f). Most of the carbide precipitates were observed in the size range of ~50–150 nm, which were much smaller than those in the casting or wrought Co-Cr-Ni-W alloy [35,36]. The ε-Co phase cannot be observed in the two claddings before the TF test due to the rapid cooling by laser deposition and the increase in the Ni content, which enhance the γ-Co phase at room temperature.

3.2. Mechanical and thermal-fatigue properties of coating

The micro-hardness distribution curves of the two claddings along the depth are shown in Fig. 8. Some characteristics could be found in the two deposition layers: the maximum hardness appeared at the subsurface and closed to the value of the H13 steel when the base metal was reached. In addition, the hardness of the double layer close to the

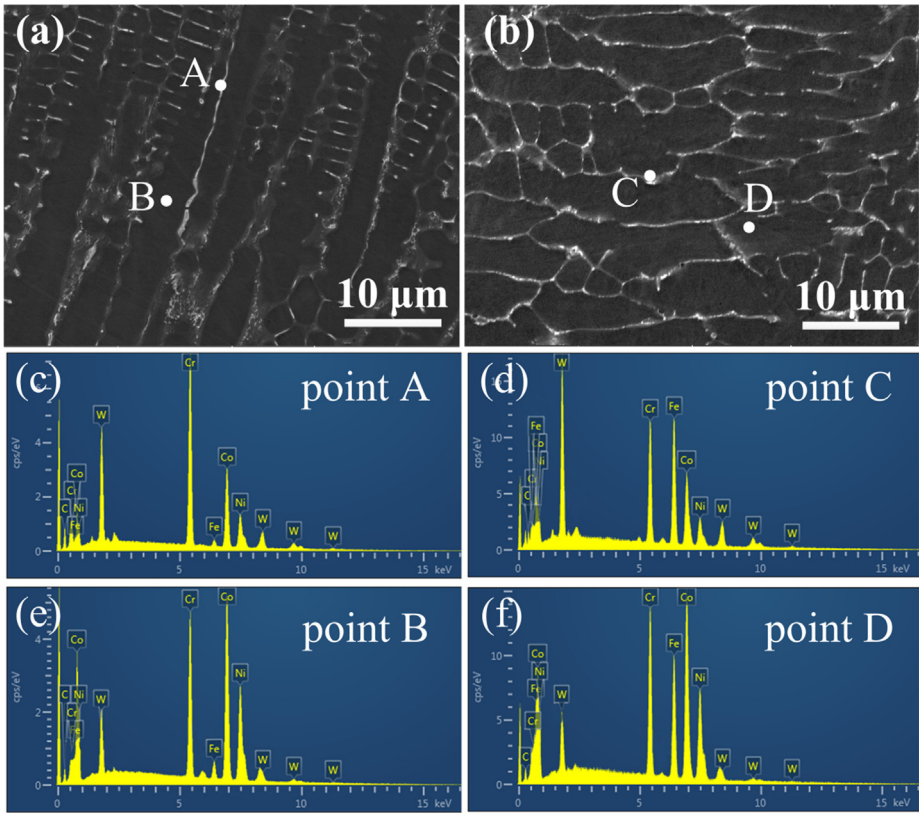

Fig. 4. Back-scattered electron micrographs of the (a) double cladding and (b) single cladding, the EDS analysis for (c) A (d) C (e) B (f) D points.

Table 3
EDS analysis of the chemical compositions at the location marked in Fig. 4 (wt. %).

Location	Co	Ni	Cr	W	Fe	C
A	27.59	15.98	31.59	19.96	4.74	0.14
B	39.67	25.29	19.97	10.27	4.12	0.68
C	12.95	9.89	19.77	28.72	27.88	0.79
D	35.42	21.16	17.33	7.98	17.63	0.48

base metal was different from that of the single layer, which was considerably soft. As depicted in Fig. 9, the two layers had different variation tendency in hardness during the TF process. Specifically, the hardness of the double cladding remained unchanged before 1300 cycles and subsequently declined. This indicated that the γ phase was excellently stable during the TF test, and the increase in the porosity led to a reduction in the hardness owing to the cracks [37]. Conversely, the single-layer hardened during the TF test and softened after the crack initiation. Some reports investigated the relationship between the structure evolution and hardness variation. The hardness increased slightly because of the transformation of the γ phase to the ε phase [38,39]. Fig. 10 presents the relationship between the TF number and the crack width, which illustrates the stability of the TF for claddings [40]. The critical TF cycles of the double layer were approximately 1300 and were considerably more than that of the single layer (about 600 cycles). The critical TF test numbers were defined by the appearance of a small "hole," which implied the early destruction on the surface, and the cracks initiated from the hole developed (Fig. 11). Moreover, the crack width of the two layers increased as the TF cycles increased. The TF cracks in the single layer showed a faster growth rate than those in the double layer.

3.3. Microstructure evolution during the TF process

The destruction processes of the two samples are shown in Fig. 11. Under the sustained thermal stress, the cracks propagated a broken line instead of a straight one, and the precipitates and grain boundaries altered the developed direction of the crack, which could be extended toward less energy. Fig. 11(c) and (d) show the crack propagation pathway of the double layer in the matrix and precipitate phases, and the break line was approximately perpendicular to the laser deposition direction due to its high residual stress [41]. However, it was difficult to observe the cracks propagated along the interface or grain boundary owing to the large width. The crack initiation and the development mechanism of the single layer were similar to those of the double layer; however, the cracks at the single layer appeared relatively short and exceedingly dispersive (Fig. 11(g) and (h)). The stress direction was in accordance with that of deposition and perpendicular to the crack direction. It could be confirmed in Fig. 12(d)–(f) that the preferred positions of the crack tip were the grain and γ/ε phase boundaries. The cracks at the double layer were longer and more continuous than those of the single layer. This was caused by the residual stress level. The residual stress was not freed until the hole-defect or micro-crack formed, implying that the residual stress increased as the number of TF tests increased. The results indicated that the duplex layer suffered higher tensile stress than the single one because of the extra TF test and it led to further drastic crack propagation. Furthermore, by contrast with the original, in Fig. 6, the ε-Co phase appeared in the single layer after TF owing to the γ/ε martensitic transformation, although no phase change occurred in the structure of the double cladding (Fig. 12(b)). Meanwhile, the LOM map (Fig. 12(f)) shows that the residual stress was concentrated on the ε-Co phase and grain boundary.

From the XRD results (Fig. 13(b)), it was verified that the single cladding contained strong diffraction peaks of ε phase after TF treatments. Fig. 13(a) reveals that the phase composition remained original in the duplex layer. It is noticeable that only the γ-Co and $M_{23}C_6$ phases

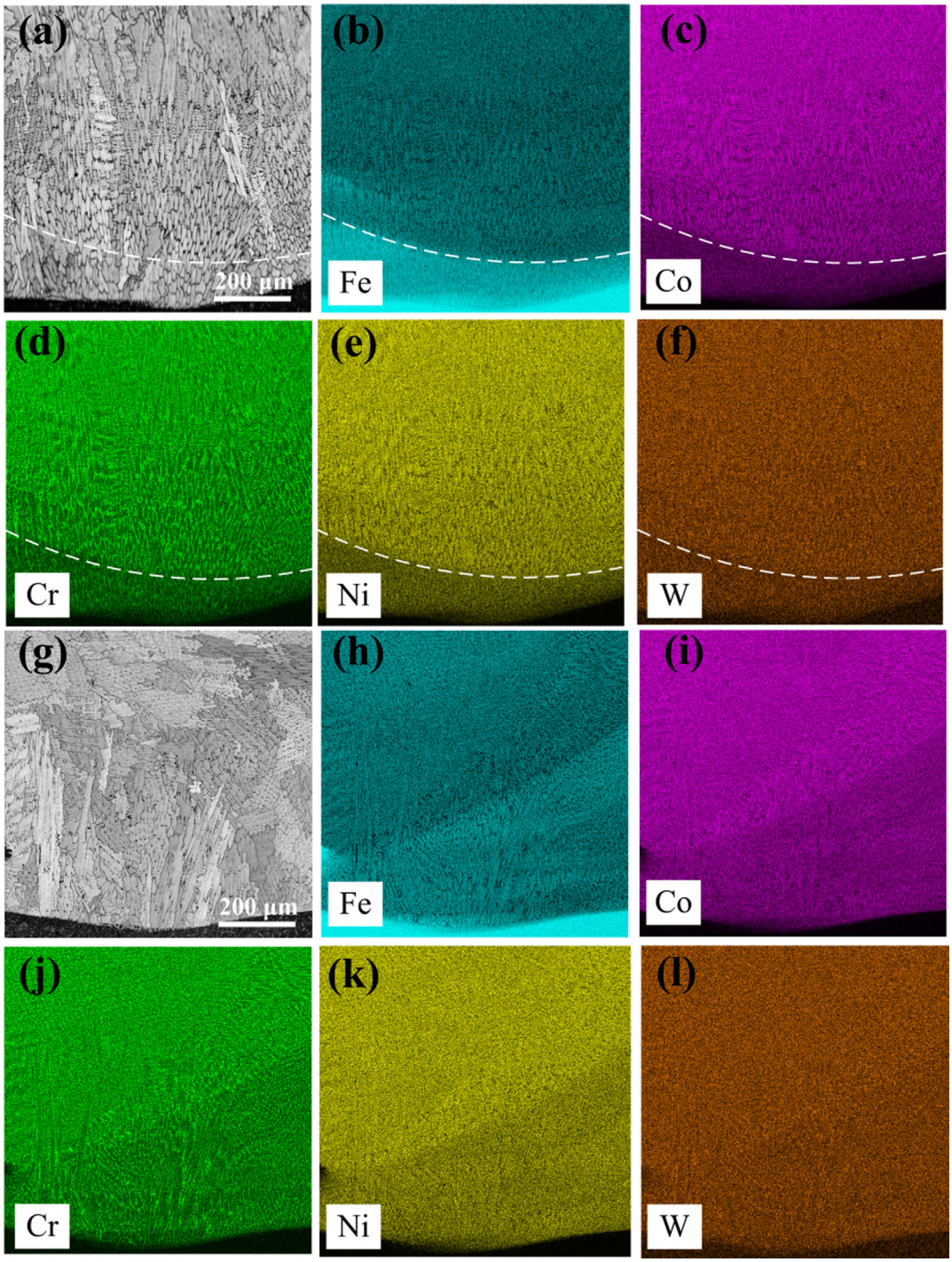

Fig. 5. SEM images of cladding and element distributions of Fe, Co, Cr, Ni, and W. (a)–(f) of the double layer and (g)–(l) of the single layer.

existed on the two samples before the TF test, which is in accordance with the prior results of TEM and EBSD. Fig. 14(a) is a bright-field TEM micrograph of the structure at the TF surface of the duplex layer and the SAED pattern, which show the γ-Co and $M_{23}C_6$ phases with [0 1 1] and [22]$\bar{1}$ axes, respectively (Fig. 14(b) and (c)). The microstructure of the single layer consisted of γ-Co, ε-Co, and $M_{23}C_6$ phase reflections in Fig. 14(d); the ε-Co phase reflection was very thin and grew along the matrix interface. It could be observed that the S-N relationship ($[0\ 1\ 1]_\gamma//[1\ 1\ \bar{2}\ 0]_\varepsilon$ and $(1\ \bar{1}\ 1)_\gamma//(0\ 0\ 0\ \bar{1})_\varepsilon$) consisted of ε-Co and γ-Co phases (Fig. 14(e) and (f))[18]; the ε-Co phase was initiated by the strain-induced martensitic transformation of the γ-Co phase due to the low SF energies. The TEM results of the two samples corresponded well with the displayed phase in XRD.

4. Discussion

4.1. Effect of alloy elements on the properties

According to previous investigations, the two types of deposition layers were constituted by the γ-Co phase and $M_{23}C_6$ phase; however, there were many differences in the hardness and critical TF life for the two claddings [42,43]. This difference must be linked with the dissimilitude in the microstructures of the two samples surfaces; in addition, the alloy element played an important role. The elements from the

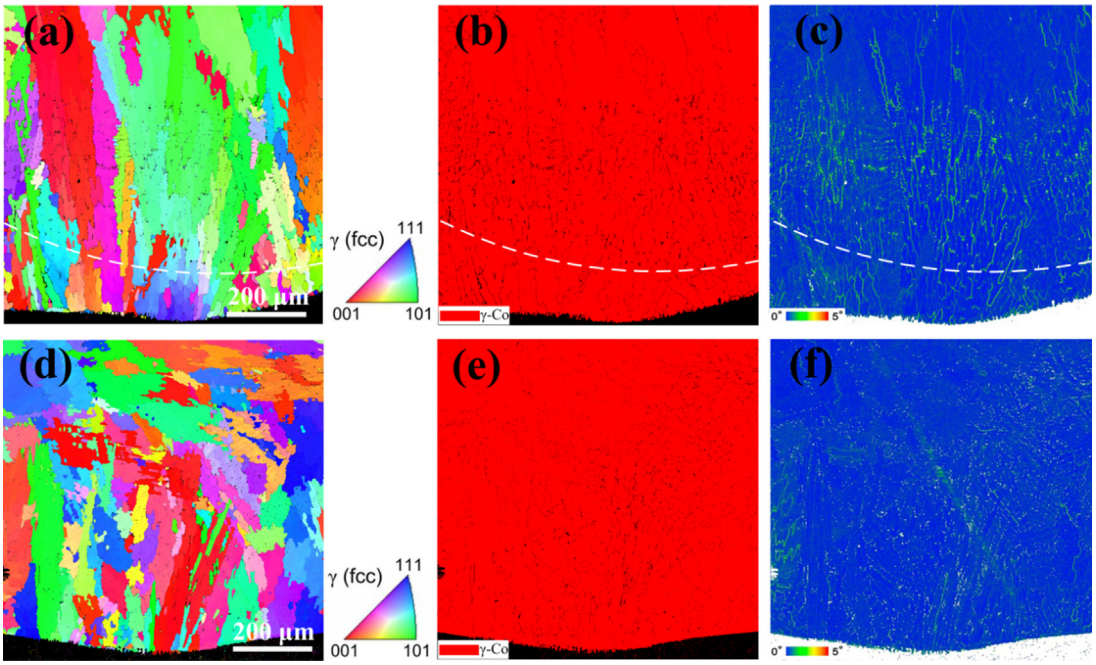

Fig. 6. EBSD analysis of the IPF, phase, and LMO maps of (a)–(c) the double layer and (d)–(f) the single layer.

base metal can be hindered by the second deposition, as described in Fig. 5. Taking no account of the H13 steel dissolution, the γ-Co phase mainly contained Ni, Cr, and W elements. Generally, the parent metal offered a mass of Fe and a few C and Cr elements. All the elements induced a lattice distortion of the γ-Co phase due to the substitutional or interstitial solid solution. The variation on the lattice parameters was studied by XRD in Fig. 12. The diffractograms exhibited (1 1 1), (2 0 0), and (2 2 0) peaks of the γ-Co phase within the range of the diffraction angle, 2θ. The dotted lines showed the standard reference that followed the lattice parameter, a_0 = 0.35442 nm of the γ-Co phase. The XRD peaks of the experiment shifted toward the lower angles in the two claddings, thereby revealing the expansion of the lattice, which increased the distance between the internal atoms [44–46]. As listed in Table 4, the lattice parameter of the double layer revealed a larger expansion than that of the single one, which might be linked mainly with the interstitially dissolved carbon. Carbon, owing to its small atomic radius, could pass into the interstitial sites in the fcc structure instead of the substitutional solid solution to large atoms such as Ni, Fe, Cr, and Si. For the strengthening effect, the former was better than the latter, which resulted in a relatively large distortion, although other elements could also enlarge the lattice parameter. The base metal with a low carbon content (0.37 wt%) could reduce the carbon content in the coating (0.7 wt% original), and the increased quantity of precipitate formed in the single layer also weakened the reinforcement effect of the interstitial solid solution in the γ-Co phase matrix. The solution strengthening of C in the fcc structure has been confirmed already, and the linear relation existed in the lattice change, carbon content, and yield strength [47]. The two factors resulted in the relatively high hardness of the double coating and resulted in enhanced resistance to TF.

The coatings suffered from the cyclic thermal stress during the TF process, and the microstructure and phase transformations could affect

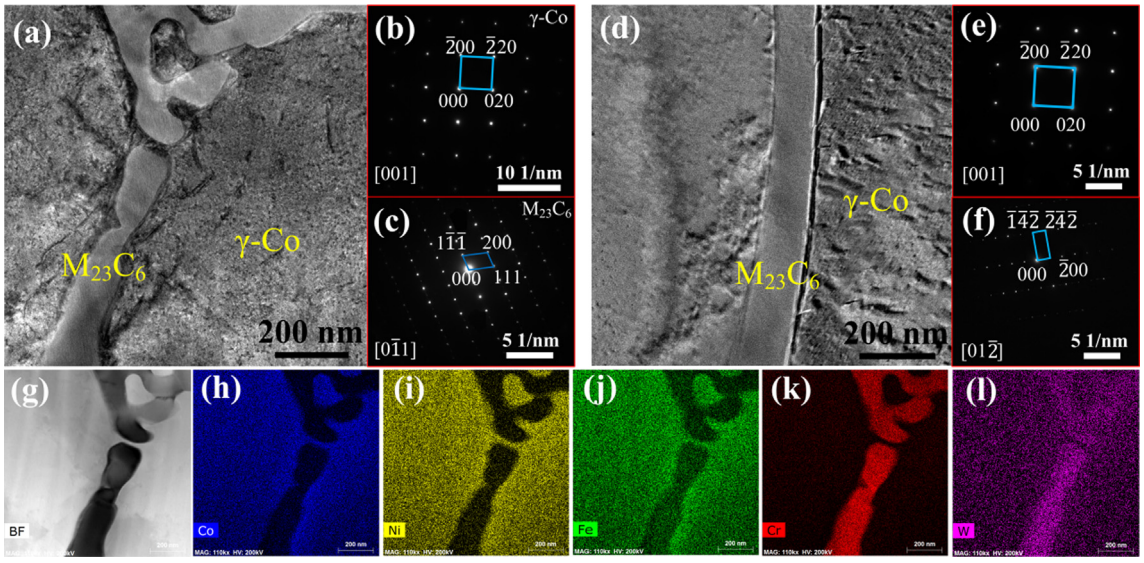

Fig. 7. TEM analysis of coatings: bright-field image; SEAD patterns of (a)–(c) the double layer and (d)–(f) the single layer. TEM–EDS analysis of the (g) double cladding bright-field image, (h) Co, (i) Ni, (j) Fe, (k) Cr, and (l) W.

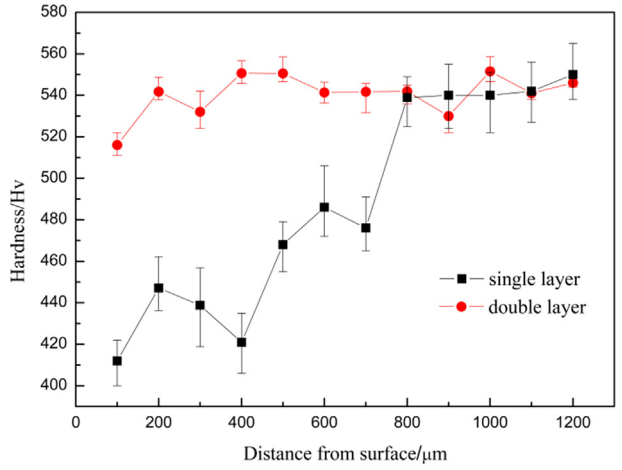

Fig. 8. Micro-hardness distribution curves of the double and single layers.

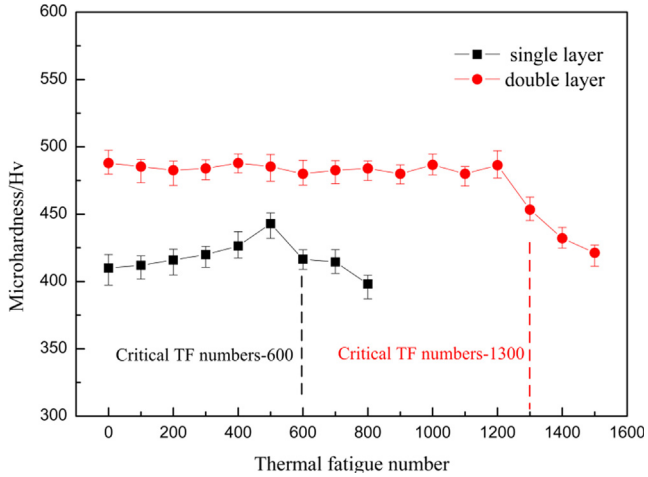

Fig. 9. Micro-hardness of the double and single layer surfaces at different TF cycles.

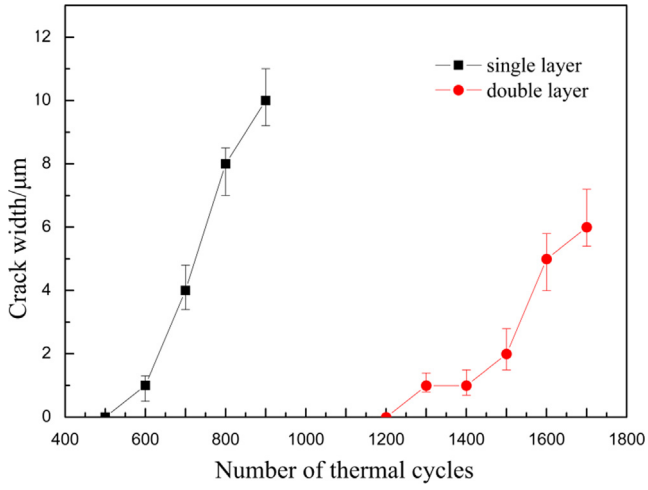

Fig. 10. Variation in the thickness of the cracks during the TF process.

the resistance to the TF. The martensitic transformation of γ/ε occurred at approximately 900 °C according to the phase diagram [47]; however, the strain triggered the transformation at a relatively low temperature as the aforementioned SIMTs. Specifically, the dissolved Fe atoms reduced the Ni content of the γ-Co matrix, which facilitated the change. Fig. 12 shows that the cracks tended to initiate from the interface, indicating that the carbide and ε phases exhibit lower fracture toughness than the γ-Co phase matrix. This confirmed that the stability of the γ phase was beneficial to restraining the crack, particularly with the increase in the number of elements, which can improve the resistance of the fcc structure and help moderate the formation of the cracks. From this viewpoint, it appeared that the multi-layer structure and increase in Ni content were good for resisting the thermal damage.

4.2. Effect of alloy elements on martensitic transformation

The influence of alloy elements in martensitic transformation could be described by SF energies, which was the most important factor of determining whether twinning, martensitic transformation, or dislocation glide alone could occur under stress [48]. If the SF energies were low, the perfect dislocations were easily decomposed into two partial dislocations and SF, the distance of slip surface increased and the climbing and cross-slip were hard, which led to the extended dislocation aggregated difficultly. The twinning began to coordinate deformation resulted in the conducive orientation to deformation. The SF became the nucleus of the martensitic transformation if the energies were quite low [49]. In contrast, the perfect dislocations were not easily decomposed and they could move through cross-slip before forming tangles with other dislocations if SF energies were high, the deformation was led by dislocation. Generally, the phase transformation of the fcc metal was favored over twinning when the SF energies were low (< 18 mJm^{-2}) and preferred to the dislocation glide at a relatively high SF energies (> 45 mJm^{-2}) [50].

Carbon could enhance the solid solution strengthening significantly and impact the SF energies noticeably. Carbon could improve the stability of the γ-Co and increase the SF energies of the Stellite 6 alloy [51]. Otherwise, carbon could also improve the SF energies of the FeCrMn alloy systems [52]. It is well known that Cr and W could reduce the SF energies of γ-Co, although Ni and Fe could increase the value of the SF energies [22,48].

The SFE could be calculated using the Jmatpro software and measured by XRD [51]. The experiment method can be expressed by Eq. (1), according to Reed and Schramn [53]:

$$\gamma_{SFE} = \frac{K_{111}\omega_0 G_{111} a_0}{\pi\sqrt{3}} A^{-0.37} \frac{\langle \varepsilon_{50}^2 \rangle_{111}}{\alpha}, \quad (1)$$

where $K_{111}\omega_0$ is a constant, determined by crystal geometry; G_{111} is the shear modulus in the (1 1 1) fault plane; a_0 is the lattice constant. $\langle \varepsilon_{50}^2 \rangle_{111}$ is the root mean square microstrain in the [1 1 1] direction averaged over a distance of 50 Å; $A^{-0.37}$ is the elastic anisotropy correction factor, and α is the stacking fault probability.

Consequently, Eq. (1) could be simplified as follows:

$$\gamma_{SFE} = K \times \frac{\langle \varepsilon_{50}^2 \rangle_{111}}{\alpha}. \quad (2)$$

The relationship between the peak shift and α has been conducted by Warren as expressed in Eq. (3), and it illustrates the peak separation, which is caused by the stacking fault [51]:

$$\Delta(2\theta_{200} - 2\theta_{111}) = \frac{-90\sqrt{3}\alpha}{\pi^2}\left(\frac{\tan\theta_{200}}{2} + \frac{\tan\theta_{111}}{4}\right), \quad (3)$$

$$\Delta(2\theta_{200} - 2\theta_{111}) = (2\theta_{200} - 2\theta_{111}) - (2\theta_{200}^0 - 2\theta_{111}^0), \quad (4)$$

where $2\theta_{200}$ and $2\theta_{111}$ are the angles of the (2 0 0) and (1 1 1) crystal faces (Fig. 13), which are influenced by the SF energies. Moreover, θ_{200}^0 or $2\theta_{111}^0$ is the angle of (2 0 0) or (1 1 1) without faults, and it is difficult to obtain by experiment directly. Therefore, the parameters are calculated using Eq. (5)–(7), which were deduced by Rong and He [54]:

$$C = \Delta 2\theta_{200}/\Delta 2\theta_{111} = -2\tan\theta_{200}/\tan\theta_{111}, \quad (5)$$

$$2\theta_{200}^0 - 2\theta_{111}^0 C = 2\theta_{200} - 2\theta_{111} C = Q, \quad (6)$$

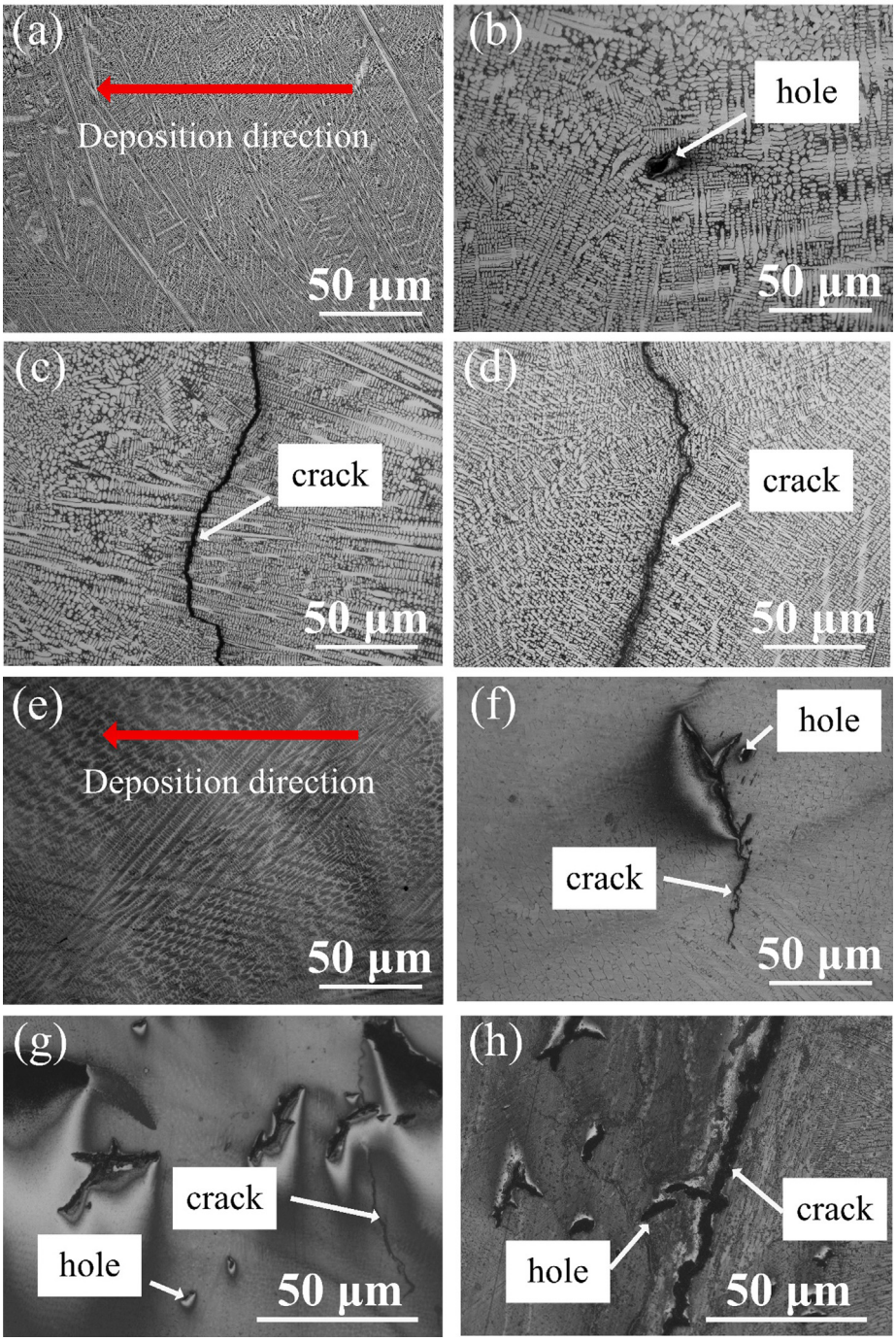

Fig. 11. Cracks initiation of the double layer after TF testing cycles of (a) 1200, (b) 1300, (c) 1400, and (d) 1500; the variation in the single-layer surface after TF testing cycles of (e) 500, (f) 600, (g) 700, and (h) 800.

$$2\sin^{-1}\left(\frac{\lambda}{a}\right) - 2\sin^{-1}\left(\frac{\sqrt{3}\lambda}{2a}\right)\frac{180}{\pi} = Q, \tag{7}$$

where C is the proportion between $\Delta 2\theta_{200}$ and $\Delta 2\theta_{111}$, and Q is a constant. The α values of the two claddings were calculated using the Matlab software, as listed in Table 5. The fact was that the α value of the double layer was less than that in the single one. Moreover, the SF energies were calculated using the Jmatpro software, and the results are shown in Fig. 15. It revealed that there was a near-linear relationship between the SF energies and the temperature, which had been verified in other alloys [50,55]. The SF energies of the double and single layers were about 26.6 mJm^{-2} and 37.3 mJm^{-2} at room temperature. The above results indicated that the double layer had higher SF energies and less formation of the SF probability (α) than those of the single layer. It also implied that the former had lower probability of γ/ε transformation than the latter. According to the theoretical calculation, it was observed that the two layers could be stabilized at the γ-Co phase during the TF process because the SF energies were higher than the threshold (< 18 mjm^{-2}). The uneven components in the matrix had an effect on the actual SF energies, which were lower than the value from the theoretical calculation. For instance, the vicinities of the grain boundaries concentrated mainly on Cr and W, which led to the reduction of the SF energies and promotion of the γ/ε transformation, as observed in the test (Fig. 14). Based on the statistical data and calculated results of the SF energies, the single cladding tended toward

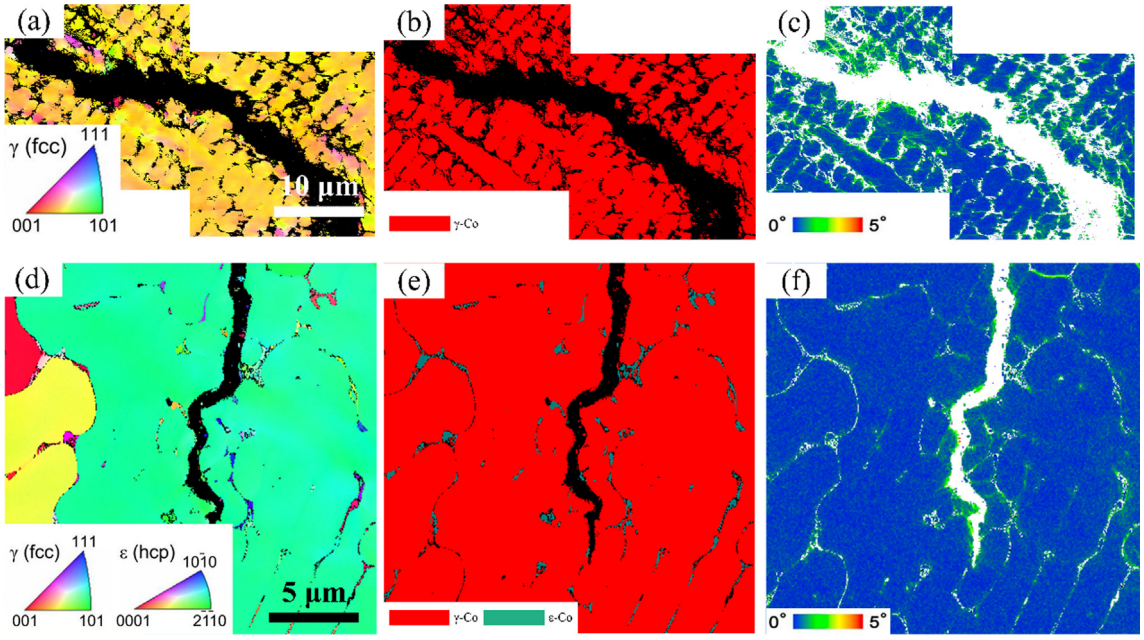

Fig. 12. EBSD analysis of the IPF, phase, and LMO maps for the cracks of (a)–(c) the double layer and (d)–(f) the single layer.

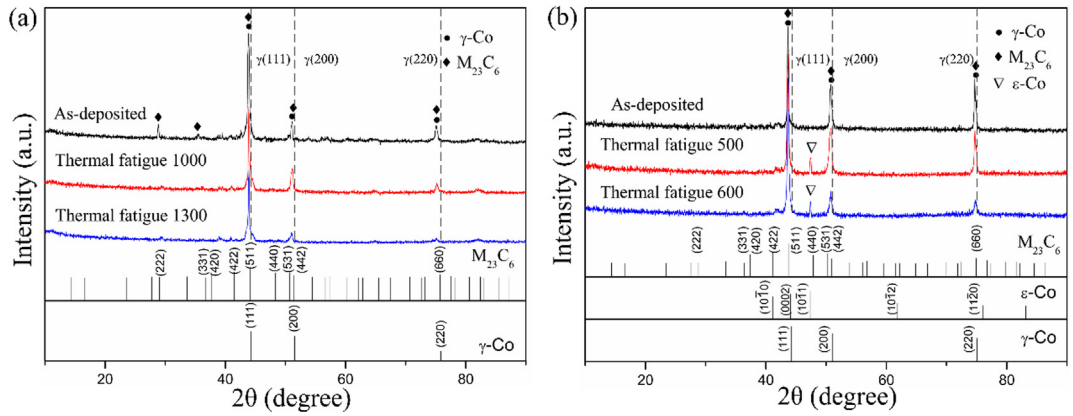

Fig. 13. XRD of the two claddings in laser deposition and after the TF test of the (a) double layer and (b) single layer.

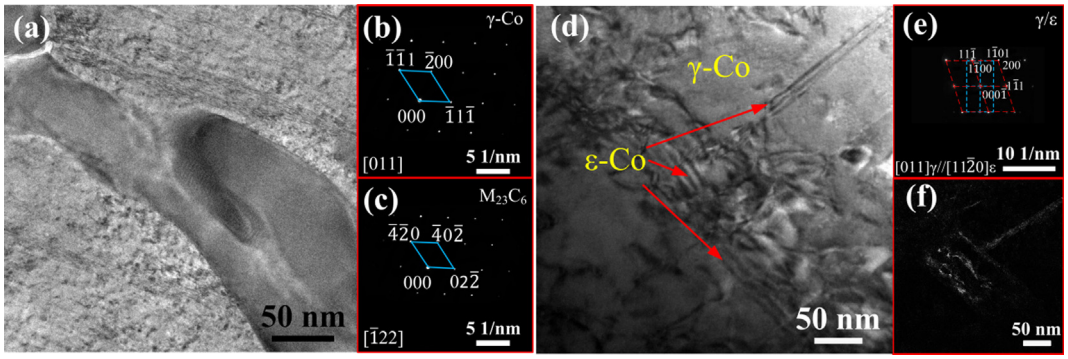

Fig. 14. TEM analysis of the coatings after the TF test: bright-field image and SEAD patterns of (a)–(c) the double layer and (d)–(e) the single layer, (f) dark field image showing the ε-Co phase.

Table 4
Lattice parameters of the double and single claddings (nm).

Sample	Original lattice parameter	Lattice parameter after cladding
Double layer	0.35442	0.35932
Single layer	0.35442	0.35724

SIMTs and formed a ε-Co phase under the cycle stress during the TF test.

4.3. Crack initiation and propagation mechanism

The TF was one of the main failure forms that caused the hot-work die-steel to lose efficacy, and it involved nucleation, propagation, and

Table 5
SF probability of the two claddings.

No.	hkl	2θ/deg.	a_0/nm	$2\theta^0$/deg.	α ($\times 10^{-3}$)
1	111	43.605	0.35932	43.595	6.61
	200	50.754		50.779	
2	111	43.861	0.35724	43.847	8.84
	200	51.045		51.078	

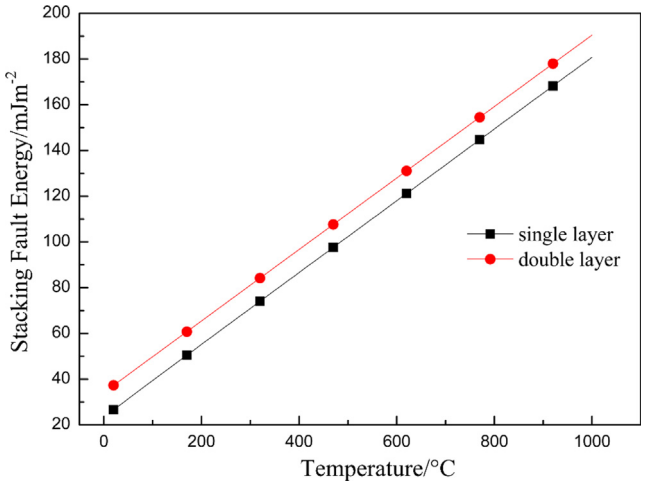

Fig. 15. SF energies of the double and single layers obtained using Jmatpro.

rapid growth, which reflected the surface roughness reduction of the products in addition to the structural failure. The research focused on the key factors, which accelerated the crack initiation and attempted to improve the TF life of the molds by overcoming these shortcomings. Meanwhile, the modification of the crack gestation and location was efficient for increasing the work-life and reducing the risk. The TF course did not tend to accumulate the residual stresses until the crack was formed, indicating that subtle changes in the surface would bring about rapid and acute crack growth. The cracks were born in the surface and pregnant period was restrained. The existence of a hole before the cracks appeared made it possible to monitor the crack nucleation, and repair measures could be employed immediately. The sketch maps of the cracks initiation and propagation are shown in Fig. 16.

In the early stage, the oxidation of the surface microstructure was attributed to the cycle of induction-heat and water-cooling, and it could prevent further oxidation.

The carbides along the grain boundaries were oxidized easily compared to those in the matrix because of the high diffusion coefficient of Cr [56,57]. The precipitates suffered from the extrusion and shrinkage from the Co phases due to the difference between the expansion coefficients during the TF process. The micro-cracks (hole) were formed when the precipitate separated from the matrix and the oxidation diffused into the coating from the defect. As a result of the stress concentration, the cracks could aggravate rapidly from the hole under the circulation of oxidation and stress [58]. Therefore, a high level of oxygen content was located near the cracks (Fig. 16(f)).

The interfaces in the grain boundary and phase boundary were responsible for the nucleation of the cracks at high cycle thermal stress amplitudes. The duplex deposition and increment of the Ni content can reduce the amount of carbides and the ε-Co phase, which can, in turn, improve the TF resistance of the hot-work mold.

5. Conclusions

The TF evaluation of Co-based coating on the AISI H13 steel modified by laser deposition with double and single layers was performed, mainly concentrating on the crack initiation. The conclusions could be summarized as follows:

(1) The double and single claddings identically consisted of the γ-Co matrix and $M_{23}C_6$ precipitate, which contained W and Cr, in addition to columnar, cellular, and dendritic grains. Additional carbide species existed on the surface of the single layer owing to the element diffusion of the base metal.
(2) The γ to ε martensitic transformation only occurred in the single cladding due to the stability degradation of the γ-Co phase and the decrease in the SF energies, which was caused by the alloy element diffusion of the base metal.
(3) The oxidation occurred early in the TF test, and the micro-crack did not appear until the thermal residual stress separated the carbides or the ε phase from the matrix. The grain boundaries and the γ/ε phase boundaries acted as the weak area for the crack initiation. The two laser deposition layers reduced the content of the carbides and restrained the phase transformation, which led to relatively high critical TF cycles.

CRediT authorship contribution statement

Xudong Yang: Methodology, Visualization, Data curation, Writing - original draft.. **Chuanwei Li:** Investigation, Project administration, Writing - review & editing. **Ziyang Zhang:** Software, Validation. **Xinyu Zhang:** Formal analysis. **Jianfeng Gu:** Supervision, Funding acquisition, Resources, Writing - review & editing.

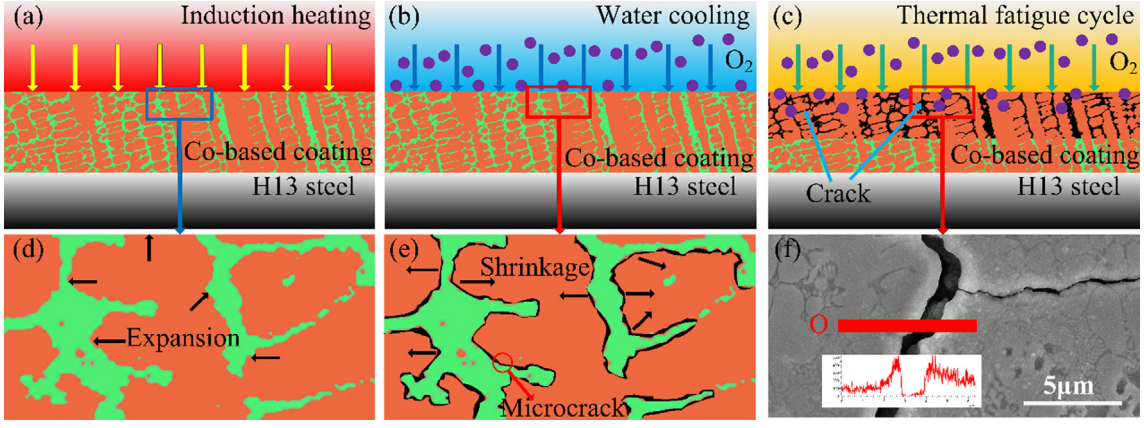

Fig. 16. Diagrammatic drawing of the TF process: (a) and (d) before the appearance of the cracks, (b) and (e) crack initiation, (c) and (f) crack propagation.

Declaration of Competing Interest

The authors declare that they have no known competing financial interests or personal relationships that could have appeared to influence the work reported in this paper.

Acknowledgment

This was work supported by the National Natural Science Foundation of China (Grant No.51801126, No.51971145) and the National Key Research and Development Program of China (Grant No. SQ2018YFB200007).

References

[1] X. Tong, M.J. Dai, Z.H. Zhang, Thermal fatigue resistance of H13 steel treated by selective laser surface melting and CrNi alloying, Appl. Surf. Sci. 271 (2013) 373–380, https://doi.org/10.1016/j.apsusc.2013.01.209.
[2] B. Wang, X. Zhao, W. Li, M. Qin, J. Gu, Effect of nitrided-layer microstructure control on wear behavior of AISI H13 hot work die steel, Appl. Surf. Sci. 431 (2018) 39–43, https://doi.org/10.1016/j.apsusc.2017.03.185.
[3] P. Zhang, C. Meng, H. Zhou, D. Cong, F. Tan, C. Wang, Z. Zhang, Y. Zhao, Tensile property of a hot work tool steel prepared by biomimetic coupled laser remelting process with different laser input energies, Appl. Surf. Sci. 258 (2012) 8732–8738, https://doi.org/10.1016/j.apsusc.2012.05.082.
[4] D. Cong, H. Zhou, Z. Ren, Z. Zhang, H. Zhang, C. Meng, C. Wang, The thermal fatigue resistance of H13 steel repaired by a biomimetic laser remelting process, Mater. Des. 55 (2014) 597–604, https://doi.org/10.1016/j.matdes.2013.09.076.
[5] C. Wang, H. Zhou, N. Liang, C. Wang, D. Cong, C. Meng, L. Ren, Mechanical properties of several laser remelting processed steels with different unit spacings, Appl. Surf. Sci. 313 (2014) 333–340, https://doi.org/10.1016/j.apsusc.2014.05.211.
[6] Z. Jing, H. Zhou, P. Zhang, C. Wang, C. Meng, D. Cong, Effect of thermal fatigue on the wear resistance of graphite cast iron with bionic units processed by laser cladding WC, Appl. Surf. Sci. 271 (2013) 329–336, https://doi.org/10.1016/j.apsusc.2013.01.193.
[7] J. Jones, M. Whittaker, R. Buckingham, R. Johnston, M. Bache, D. Clark, Microstructural characterisation of a nickel alloy processed via blown powder direct laser deposition (DLD), Mater. Des. 117 (2017) 47–57, https://doi.org/10.1016/j.matdes.2016.12.062.
[8] C. Yang, X. Cheng, H. Tang, X. Tian, D. Liu, Influence of microstructures and wear behaviors of the microalloyed coatings on TC11 alloy surface using laser cladding technique, Surf. Coatings Technol. 337 (2018) 97–103, https://doi.org/10.1016/j.surfcoat.2017.12.058.
[9] M. Rodríguez Ripoll, C. Gachot, S. Slawik, H. Torres, B. Prakash, Microstructural design of self-lubricating laser claddings for use in high temperature sliding applications, Surf. Coatings Technol. 337 (2017) 24–34, https://doi.org/10.1016/j.surfcoat.2017.12.060.
[10] D. Gu, C. Ma, In-situ formation of Ni4Ti3precipitate and its effect on pseudoelasticity in selective laser melting additive manufactured NiTi-based composites, Appl. Surf. Sci. 441 (2018) 862–870, https://doi.org/10.1016/j.apsusc.2018.01.317.
[11] Z. Zhang, T. Yu, R. Kovacevic, Erosion and corrosion resistance of laser cladded AISI 420 stainless steel reinforced with VC, Appl. Surf. Sci. 410 (2017) 225–240, https://doi.org/10.1016/j.apsusc.2017.03.137.
[12] C. Zhao, D. Stewart, J. Jiang, F.P.E. Dunne, A comparative assessment of iron and cobalt-based hard-facing alloy deformation using HR-EBSD and HR-DIC, Acta Mater. 159 (2018) 173–186, https://doi.org/10.1016/j.actamat.2018.08.021.
[13] B.S. Lee, H. Matsumoto, A. Chiba, Fractures in tensile deformation of biomedical Co-Cr-Mo-N alloys, Mater. Lett. 65 (2011) 843–846, https://doi.org/10.1016/j.matlet.2010.12.007.
[14] J.W. Christian, The theory of transformations in metals and alloys, Theory Transform. Met. Alloy. 992 (2007) 992–1061, https://doi.org/10.1016/b978-008044019-4/50027-1.
[15] Y. Birol, Thermal fatigue testing of Stellite 6-coated hot work tool steel, Mater. Sci. Eng., A 527 (2010) 6091–6097, https://doi.org/10.1016/j.msea.2010.06.015.
[16] E. Zinutti, L. Emanuelli, M. Pellizzari, A. Molinari, F. Castellani, Thermal fatigue behaviour of WC-20Co and WC-30(CoNiCrFe) cemented carbide, Int. J. Refract Metal Hard Mater. 60 (2016) 118–124, https://doi.org/10.1016/j.ijrmhm.2016.06.014.
[17] P. Tunthawiroon, Y. Li, Y. Koizumi, A. Chiba, Strain-controlled iso-thermal fatigue behavior of Co–29Cr–6Mo used for tooling materials in Al die casting, Mater. Sci. Eng., A 703 (2017) 27–36, https://doi.org/10.1016/j.msea.2017.07.047.
[18] Y. Wu, Y. Liu, H. Chen, Y. Chen, H. Li, W. Yi, Microstructure evolution and crack propagation feature in thermal fatigue of laser-deposited Stellite 6 coating for brake discs, Surf. Coatings Technol. 358 (2019) 98–107, https://doi.org/10.1016/j.surfcoat.2018.11.011.
[19] D. Bombač, G. Kugler, B. Markoli, M. Terčelj, Hot work roller surface layer degradation progress during thermal fatigue in the temperature range 500–700 °C, Int. J. Fatigue 104 (2017) 355–365, https://doi.org/10.1016/j.ijfatigue.2017.08.008.
[20] J. Zhang, Z. Zhao, Y. Kong, Z. Zhang, Q. Zhong, Crack initiation and propagation mechanisms during thermal fatigue in directionally solidified superalloy DZ125, Int. J. Fatigue 119 (2019) 355–366, https://doi.org/10.1016/j.ijfatigue.2018.09.001.
[21] M. Salem, S. Le Roux, G. Dour, P. Lamesle, K. Choquet, F. Rézaï-Aria, Effect of aluminizing and oxidation on the thermal fatigue damage of hot work tool steels for high pressure die casting applications, Int. J. Fatigue 119 (2019) 126–138, https://doi.org/10.1016/j.ijfatigue.2018.09.018.
[22] L.Y. Tian, R. Lizárraga, H. Larsson, E. Holmström, L. Vitos, A first principles study of the stacking fault energies for fcc Co-based binary alloys, Acta Mater. 136 (2017) 215–223, https://doi.org/10.1016/j.actamat.2017.07.010.
[23] H. Xia, X. Song, L. Li, B. Chen, C. Tan, X. Zhao, L. Xiao, J. Feng, Effect of the Ni coating thickness on laser welding-brazing of Mg/steel, J. Alloy. Compd. 769 (2018) 1042–1058, https://doi.org/10.1016/j.jallcom.2018.08.080.
[24] M. Bar-Hen, I. Etsion, Experimental study of the effect of coating thickness and substrate roughness on tool wear during turning, Tribol. Int. 110 (2017) 341–347, https://doi.org/10.1016/j.triboint.2016.11.011.
[25] A.S.C.M. D'Oliveira, P.S.C.P. Da Silva, R.M.C. Vilar, Microstructural features of consecutive layers of Stellite 6 deposited by laser cladding, Surf. Coatings Technol. 153 (2002) 203–209, https://doi.org/10.1016/S0257-8972(01)01687-5.
[26] R.E. Smallman, A.H.W. Ngan, Chapter 3 – solidification, Mod. Phys. Metall. (2014) 93–119, https://doi.org/10.1016/B978-0-08-098204-5.00003-1.
[27] C. Li, R. White, X.Y. Fang, M. Weaver, Y.B. Guo, Microstructure evolution characteristics of Inconel 625 alloy from selective laser melting to heat treatment, Mater. Sci. Eng., A 705 (2017) 20–31, https://doi.org/10.1016/j.msea.2017.08.058.
[28] Z. Tong, X. Ren, J. Jiao, W. Zhou, Y. Ren, Y. Ye, E.A. Larson, J. Gu, Laser additive manufacturing of FeCrCoMnNi high-entropy alloy: effect of heat treatment on microstructure, residual stress and mechanical property, J. Alloy. Compd. 785 (2019) 1144–1159, https://doi.org/10.1016/j.jallcom.2019.01.213.
[29] Z. Liu, H. Qi, Effects of substrate crystallographic orientations on crystal growth and microstructure formation in laser powder deposition of nickel-based superalloy, Acta Mater. 87 (2015) 248–258, https://doi.org/10.1016/j.actamat.2014.12.046.
[30] F. Shu, B. Yang, S. Dong, H. Zhao, B. Xu, F. Xu, B. Liu, P. He, J. Feng, Effects of Fe-to-Co ratio on microstructure and mechanical properties of laser cladded FeCoCrBNiSi high-entropy alloy coatings, Appl. Surf. Sci. 450 (2018) 538–544, https://doi.org/10.1016/j.apsusc.2018.03.128.
[31] M.U. Farooq, U. Klement, G. Nolze, The role of α- to ε-Co phase transformation on strain hardening of a Co-Cr-Mo laser clad, Mater. Sci. Eng., A 445–446 (2007) 40–47, https://doi.org/10.1016/j.msea.2006.07.068.
[32] K. Yamanaka, M. Mori, Y. Koizumi, A. Chiba, Local strain evolution due to athermal γ→ε martensitic transformation in biomedical CoCrMo alloys, J. Mech. Behav. Biomed. Mater. 32 (2014) 52–61, https://doi.org/10.1016/j.jmbbm.2013.12.019.
[33] Y. Zhang, P. Xu, C. Liu, J. Ren, H. Gong, The influence of carbides on the microstructure, grain growth, and oxidation resistance of nanostructured carbides-strengthened cobalt-based multi-track laser-cladding layers, Appl. Surf. Sci. 469 (2019) 495–504, https://doi.org/10.1016/j.apsusc.2018.11.084.
[34] J. Zhang, H. Fu, R. Hu, G. Bai, J. Li, T. Zhang, Precipitation behavior of grain boundary M23C6 and its effect on tensile properties of Ni–Cr–W based superalloy, Mater. Sci. Eng., A 548 (2012) 83–88, https://doi.org/10.1016/j.msea.2012.03.092.
[35] M. Samii Zafarghandi, S.M. Abbasi, A. Momeni, Effects of Nb on hot tensile deformation behavior of cast Haynes 25 Co-Cr-W-Ni alloy, J. Alloys Compd. 774 (2019) 18–29, https://doi.org/10.1016/j.jallcom.2018.09.301.
[36] S. Zangeneh, H.R. Lashgari, M. Asnavandi, The effect of long-term service exposure on the stability of carbides in Co–Cr–Ni–W (X-45) superalloy, Eng. Fail. Anal. 84 (2018) 276–286, https://doi.org/10.1016/j.engfailanal.2017.11.018.
[37] W.M. Tucho, V.H. Lysne, H. Austbø, A. Sjolyst-Kverneland, V. Hansen, Investigation of effects of process parameters on microstructure and hardness of SLM manufactured SS316L, J. Alloy. Compd. 740 (2018) 910–925, https://doi.org/10.1016/j.jallcom.2018.01.098.
[38] N. Tang, Y. Li, P. Tunthawiroon, Y. Koizumi, A. Chiba, Thermo-mechanical fatigue test of a wrought Co-based alloy as potential tooling material for die casting, Mater. Sci. Eng., A 615 (2014) 164–168, https://doi.org/10.1016/j.msea.2014.07.073.
[39] Y. Kajima, A. Takaichi, N. Kittikundecha, T. Nakamoto, T. Kimura, N. Nomura, A. Kawasaki, T. Hanawa, H. Takahashi, N. Wakabayashi, Effect of heat-treatment temperature on microstructures and mechanical properties of Co–Cr–Mo alloys fabricated by selective laser melting, Mater. Sci. Eng., A 726 (2018) 21–31, https://doi.org/10.1016/j.msea.2018.04.048.
[40] B. Liu, B. Wang, X. Yang, X. Zhao, M. Qin, J. Gu, Thermal fatigue evaluation of AISI H13 steels surface modified by gas nitriding with pre- and post-shot peening, Appl. Surf. Sci. 483 (2019), https://doi.org/10.1016/j.apsusc.2019.03.291.
[41] C. Lee, H. Park, J. Yoo, C. Lee, W. Woo, S. Park, Residual stress and crack initiation in laser clad composite layer with Co-based alloy and WC + NiCr, Appl. Surf. Sci. 345 (2015) 286–294, https://doi.org/10.1016/j.apsusc.2015.03.168.
[42] H. Peng, R. Li, T. Yuan, H. Wu, H. Yan, Producing nanostructured Co-Cr-W alloy surface layer by laser cladding and friction stir processing, J. Mater. Res. 30 (2015) 717–726, https://doi.org/10.1557/jmr.2015.28.
[43] Z.W. Wei, W.X. Zhao, J.Y. Zhou, C.K. Liu, Z. Zhen, S.Y. Qu, C.H. Tao, Microstructure evolution of K6509 cobalt-base superalloy for over-temperature, Procedia Eng. 99 (2015) 1302–1310, https://doi.org/10.1016/j.proeng.2014.12.663.
[44] J. Wang, Z. Li, D. Wang, S. Qiu, F. Ernst, Thermal stability of low-temperature-carburized austenitic stainless steel, Acta Mater. 128 (2017) 235–240, https://doi.org/10.1016/j.actamat.2017.02.018.
[45] G. Maistro, C. Oikonomou, L. Rogström, L. Nyborg, Y. Cao, Understanding the microstructure-properties relationship of low-temperature carburized austenitic stainless steels through EBSD analysis, Surf. Coatings Technol. 322 (2017) 141–151, https://doi.org/10.1016/j.surfcoat.2017.05.036.

[46] Z. Wang, I. Baker, Z. Cai, S. Chen, J.D. Poplawsky, W. Guo, The effect of interstitial carbon on the mechanical properties and dislocation substructure evolution in Fe 40.4 Ni 11.3 Mn 34.8 Al 7.5 Cr 6 high entropy alloys, Acta Mater. 120 (2016) 228–239, https://doi.org/10.1016/j.actamat.2016.08.072.
[47] S. Kurosu, H. Matsumoto, A. Chiba, Isothermal phase transformation in biomedical Co-29Cr-6Mo alloy without addition of carbon or nitrogen, Metall. Mater. Trans. A Phys. Metall. Mater. Sci. 41 (2010) 2613–2625, https://doi.org/10.1007/s11661-010-0273-8.
[48] R. Fussik, M. Walter, W. Theisen, S. Weber, Investigation of austenitic FeCrNi steels with regard to stacking-fault energy and thermal austenite stability, Materialia. 3 (2018) 265–273, https://doi.org/10.1016/j.mtla.2018.08.020.
[49] G.B. Olson, M. Cohen, A general mechanism of martensitic nucleation: Part I. General concepts and the FCC → HCP transformation, Metall. Trans. A. 7 (1976) 1897–1904, https://doi.org/10.1007/bf02659822.
[50] S. Curtze, V.T. Kuokkala, Dependence of tensile deformation behavior of TWIP steels on stacking fault energy, temperature and strain rate, Acta Mater. 58 (2010) 5129–5141, https://doi.org/10.1016/j.actamat.2010.05.049.
[51] D. Yang, C. Hua, S. Qu, J. Xu, J. Chen, C. Yu, H. Lu, Isothermal transformation of γ-Co to ε-Co in Stellite 6 coatings, Metall. Mater. Trans. A Phys. Metall. Mater. Sci. 50 (2019) 1153–1161, https://doi.org/10.1007/s11661-018-5057-6.
[52] R. Xiong, H. Peng, H. Si, W. Zhang, Y. Wen, Thermodynamic calculation of stacking fault energy of the Fe-Mn-Si-C high manganese steels, Mater. Sci. Eng., A 598 (2014) 376–386, https://doi.org/10.1016/j.msea.2014.01.046.
[53] R.P. Reed, R.E. Schramm, Relationship between stacking-fault energy and x-ray measurements of stacking-fault probability and microstrain, J. Appl. Phys. 45 (1974) 4705–4711, https://doi.org/10.1063/1.1663122.
[54] Y. Rong, G. He, Z. Guo, S. Chen, T.Y. Hsu, X-ray Peak-Shift Determination of Deformation Fault Probability in Fe-Mn-Si Alloys, J. Mater. Sci. Technol. 5 (2002) 459–461.
[55] H. ElRakayby, K.T. Kim, Effect of stacking fault energy on densification behavior of metal powder during hot isostatic pressing, Mater. Des. 99 (2016) 433–438, https://doi.org/10.1016/j.matdes.2016.03.057.
[56] P. Wang, S.M.L. Nai, D. Mangelinck, S.B. Tor, M. Descoins, W.Q. Toh, Z. Sun, E. Liu, Y. Kok, X.P. Tan, Carbide precipitation characteristics in additive manufacturing of Co-Cr-Mo alloy via selective electron beam melting, Scr. Mater. 143 (2017) 117–121, https://doi.org/10.1016/j.scriptamat.2017.09.022.
[57] S. Xiang, S. Mao, Z. Shen, H. Long, H. Wei, S. Ma, J.X. Zhang, Y. Chen, J. Zhang, B. Zhang, Y. Liu, Site preference of metallic elements in M23C6 carbide in a Ni-based single crystal superalloy, Mater. Des. 129 (2017) 9–14, https://doi.org/10.1016/j.matdes.2017.05.023.
[58] M. Bartsch, W. Theisen, L. Mujica Roncery, C. Meid, I. Lopez-Galilea, B. Ruttert, Effect of porosity and eutectics on the high-temperature low-cycle fatigue performance of a nickel-base single-crystal superalloy, Scr. Mater. 155 (2018) 139–143, https://doi.org/10.1016/j.scriptamat.2018.06.036.